01 Dec 2017

# Topography of the Mantle Transition Zone Discontinuities Beneath Alaska and its Geodynamic Implications: Constraints from Receiver Function Stacking

Haider H. Dahm

Stephen S. Gao
*Missouri University of Science and Technology*, sgao@mst.edu

Fansheng Kong

Kelly H. Liu
*Missouri University of Science and Technology*, liukh@mst.edu

## Recommended Citation

**Key Points:**
- The apparent depths of the 410 and 660 km discontinuities are positively correlated, suggesting strong upper mantle velocity heterogeneities
- The Pacific slab reaches the upper MTZ over a broad area beneath southern Alaska, with a possible gap with the Yakutat microplate
- The Northern Cordilleran slab window is associated with advective thermal upwelling extending to the upper MTZ

**Supporting Information:**
- Supporting Information S1
- Table S1

**Correspondence to:**
S. S. Gao,
sgao@mst.edu

# Topography of the Mantle Transition Zone Discontinuities Beneath Alaska and Its Geodynamic Implications: Constraints From Receiver Function Stacking

**Haider H. Dahm**[1,2] (ID), **Stephen S. Gao**[1] (ID), **Fansheng Kong**[1] (ID), and **Kelly H. Liu**[1] (ID)

[1]Geology and Geophysics Program, Missouri University of Science and Technology, Rolla, MO, USA, [2]Department of Geography, Misan University, Amarah, Iraq

**Abstract** The 410 and 660 km discontinuities ($d410$ and $d660$, respectively) beneath Alaska and adjacent areas are imaged by stacking 75,296 radial receiver functions recorded by 438 broadband seismic stations with up to 30 years of recording period. When the 1-D IASP91 Earth model is used for moveout correction and time depth conversion, significant and spatially systematic variations in the apparent depths of the $d410$ and $d660$ are observed. The mean apparent depth of the $d410$ and $d660$ for the entire study area is 417 ± 12 km and 665 ± 12 km, respectively, and the mean mantle transition zone (MTZ) thickness is 248 ± 8 km which is statistically identical to the global average. For most of the areas, the undulations of the apparent depths of the $d410$ and $d660$ are highly correlated, indicating that lateral velocity variations in the upper mantle above the $d410$ contribute to the bulk of the observed apparent depth variations by affecting the traveltimes of the $P$-to-$S$ converted phases from both discontinuities. Beneath central Alaska, a broad zone with greater than normal MTZ thicknesses and shallower than normal $d410$ is imaged, implying that the subducting Pacific slab has reached the MTZ and is fragmented or significantly thickened. Within the proposed Northern Cordilleran slab window, an overall thinner than normal MTZ is observed and is most likely the result of a depressed $d410$. This observation, when combined with results from seismic tomography investigations, may indicate advective thermal upwelling from the upper MTZ through the slab window.

## 1. Introduction

Subduction of the Pacific-Kula Plate beneath southern Alaska has occurred since at least 160 Ma (Fisher & Magoon, 1978; Wang & Tape, 2014). Currently, the Pacific Plate subducts beneath Alaska at a rate of about 57 mm/yr in a northwestward direction (DeMets et al., 1990). The normal subduction beneath the Aleutian trench changes to oblique beneath south central Alaska (Page et al., 1989). Based on the seismicity along the Wadati-Benioff zone, the depth of the seismogenic section of the subducting slab is about 100–150 km in south central Alaska and deepens to the west toward the central Aleutian, where it exceeds 300 km (Figure 1) (Page et al., 1995; Taber et al., 1991). The subducting Pacific slab probably joins with the Yakutat microplate along its eastern edge in the upper most mantle, but their relationship at greater depth is unclear (Eberhart-Phillips et al., 2006).

The geometry and depth extent of the aseismic section of the subducted Pacific-Yakutat Plates have been investigated by numerous seismic tomographic studies (Burdick et al., 2017; Martin-Short et al., 2016; Qi et al., 2007; Wang & Tape, 2014; Zhao et al., 1995). One of the most significant features in many of the tomographic images in central Alaska and along the Aleutians is a high-velocity zone striking NE-SW in the upper mantle (Figure 2). While some earlier studies (e.g., Qi et al., 2007) limited this high-velocity zone to the upper mantle, the most recent work (Burdick et al., 2017; Martin-Short et al., 2016) found it extending to the upper mantle transition zone (MTZ) (Figure 2), which is similar to findings from some of the global-scale tomography studies (e.g., Li et al., 2008). Whether it also exists in the lower MTZ is unclear, due to limited vertical resolution of the tomographic inversion techniques (Martin-Short et al., 2016).

Beneath the western Canadian Cordillera to the east and southeast of the Pacific-Yakutat slab assemblage, geophysical and geochemical studies have recognized a gap in the subducted Juan de Fuca and Yakutat-Pacific slabs, known as the Northern Cordilleran Slab Window (NCSW) (Figure 1) (Frederiksen et al., 1998; Thorkelson & Taylor, 1989; Thorkelson et al., 2011). The abundant volcanism above the NCSW has been regarded as the
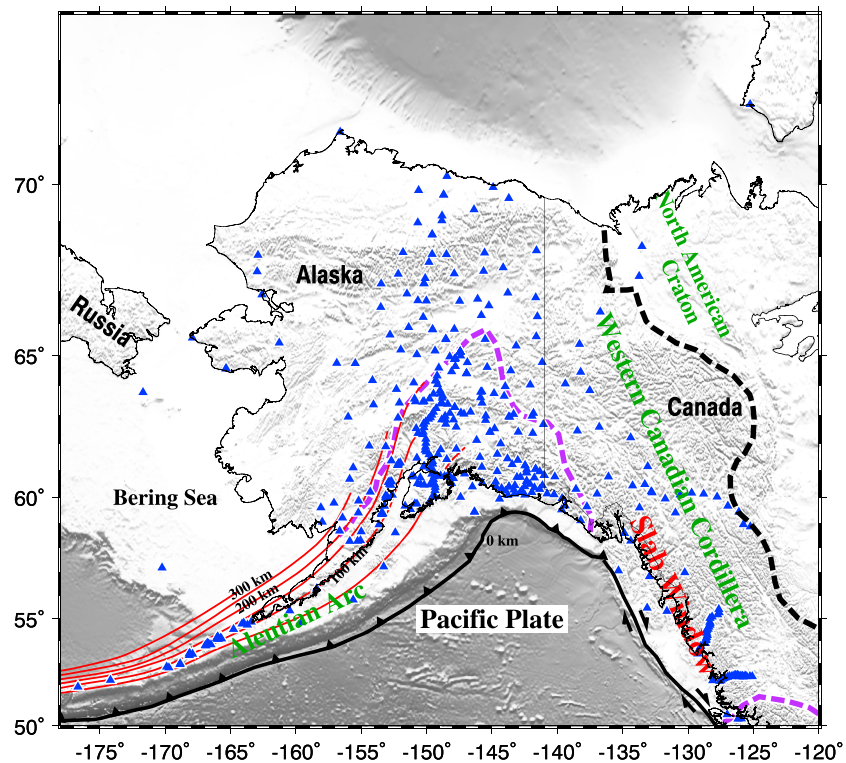
**Figure 1.** A topographic relief map of the study area showing the distribution of seismic stations used in this study (blue triangles) and contour lines of the depth of the subducting Pacific slab (red lines; the contour interval is 50 km) (Gudmundsson & Sambridge, 1998). The purple dashed line in the central part of the mapped area shows the lateral extent of the subducted Yakutat microplate, and the purple dashed line in the southeastern corner of the mapped area indicates the southern edge of a slab window (Thorkelson et al., 2011). The black dashed line defines the western boundary of the North American Craton (Yuan & Romanowicz, 2010).

consequence of the upwelling of anhydrous and hot asthenospheric mantle through the slab window (Thorkelson et al., 2011). In this area, Frederiksen et al. (1998) imaged a low-velocity zone (LVZ) that reaches 600 km depth but could be exaggerated by 100 km or more due to vertical smearing. The $P$ wave velocity anomaly reaches to about −3%, with an upper mantle average of about −2% at the center of the tabular feature which is centered at approximately 136°W by 60°N. This feature was also reported by Qi et al. (2007), but it is limited in the 0–400 km depth range, with an estimated average upper mantle $V_p$ velocity anomaly of −2%. Additionally, some continental-scale tomography studies (e.g., Schaeffer & Lebedev, 2014) show low velocities down to about 400 km beneath western Canada. The considerable uncertainty about the depth extent of this LVZ is also reflected in the recent tomographic studies shown in Figure 2 (Burdick et al., 2017; Martin-Short et al., 2016).

The discrepancies in the resulting depth extent of the velocity anomalies beneath Alaska and adjacent areas are most likely the result of a lack of sufficient raypath coverage and limited vertical resolution of the tomographic inversion techniques, as recently demonstrated by Foulger et al. (2015). Reliably determining the depth extent of velocity anomalies especially their relationship with the MTZ discontinuities can provide essential constraints on the formation mechanisms of both the high- and low-velocity anomalies. Whether the slab segments remain only in the upper mantle, have reached the $d$410, have entered the MTZ and been horizontally deflected by the $d$660 (Fukao et al., 2001), or have penetrated to the lower mantle are first-order problems related to mantle structure and dynamics (Fukao et al., 2001; Goes et al., 2017). The depth extent and geometry of subducted slab segments are closely related to the viscosity structure of the subducting slab and the ambient mantle, the density increase across the bottom of the mantle transition zone, and the age and associated density of the slab segments (Goes et al., 2017).
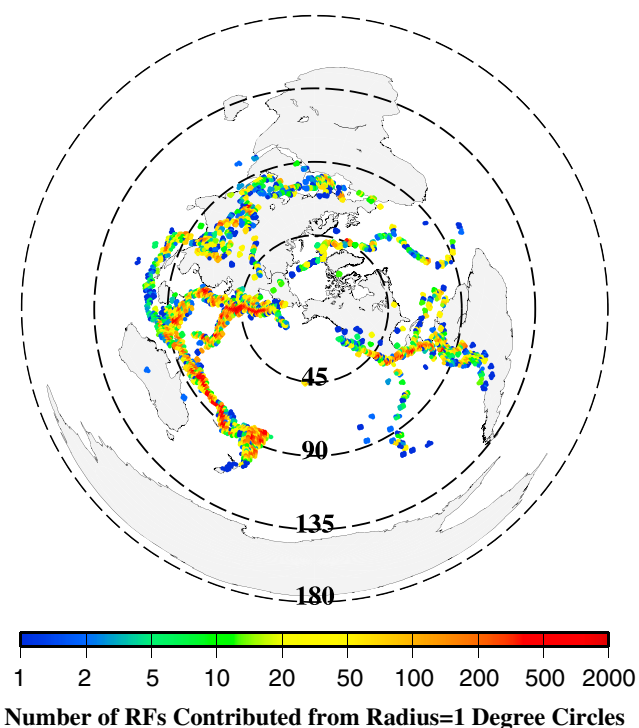
Numerous previous studies have demonstrated that the depth variations of the $d$410 and $d$660 can provide independent constraints on the depth extent of subducted cold slabs and high temperature anomalies
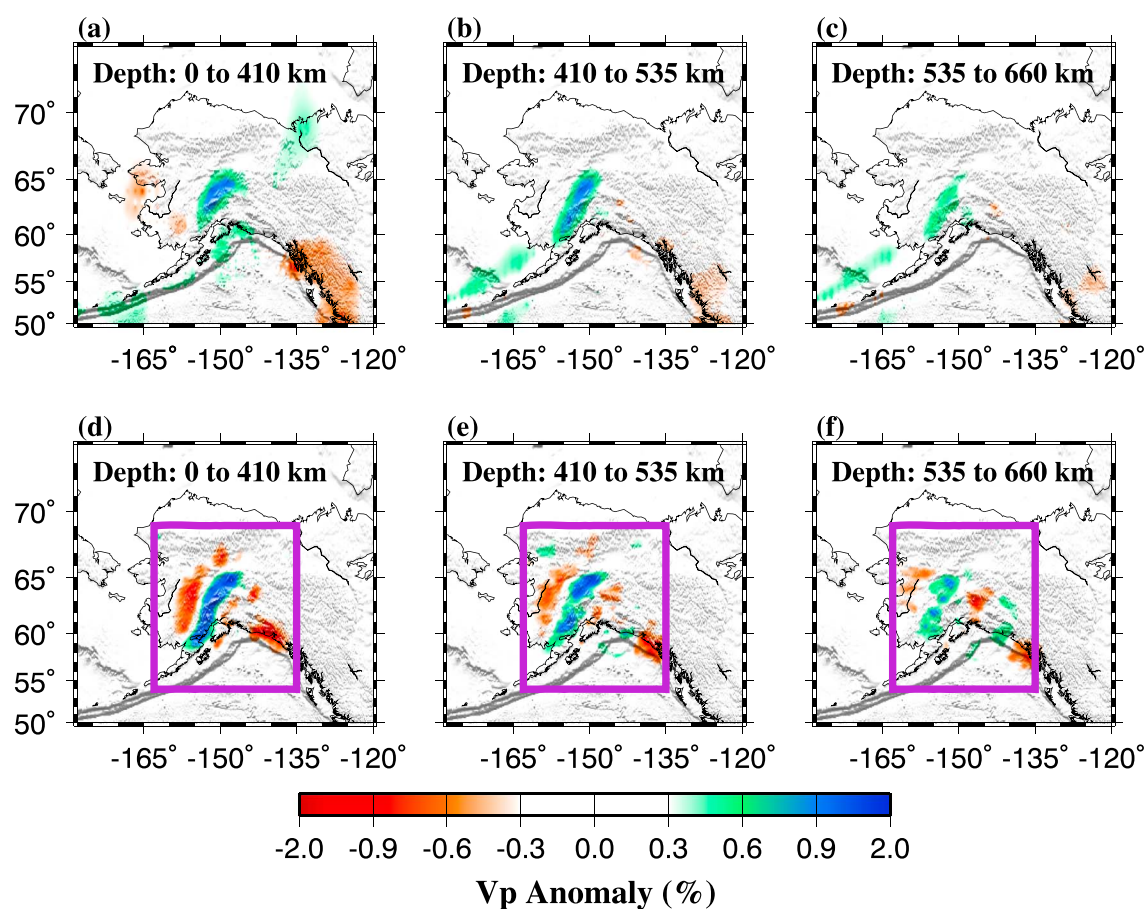
**Figure 2.** (a–c) Vertically averaged upper mantle, upper MTZ, and lower MTZ *P* wave velocity anomalies from Burdick et al. (2017). (d–f) Same as Figures 2a–2c but from Martin-Short et al. (2016), which has data only in the area confined by the purple frame.

(e.g., Anderson, 1967; Collier et al., 2001; Contenti et al., 2012; Li & Yuan, 2003; Liu et al., 2016, 2003; Shearer & Masters, 1992; Wicks & Richards, 1993; Yu et al., 2017). The d410 and d660 are ubiquitous and well established in most global models and correspond to a globally averaged MTZ thickness of 250 km (Kennett & Engdahl, 1991; Kennett et al., 1995). They are associated with mineral phase changes between $\alpha$ olivine and $\beta$ olivine at 410 km (Ringwood, 1975) and from spinel to bridgmanite at 660 km (Ito & Katsura, 1989; Yamazaki & Karato, 2001). Mineral physics experiments have indicated that the d410 and d660 have positive and negative Clapeyron slopes, respectively (Bina & Helffrich, 1994; Helffrich, 2000; Katsura et al., 2003; Fei et al., 2004), although the magnitude of the slopes is inconsistent among previous studies (see Ghosh et al., 2013 for a summary). A thicker MTZ is expected in colder regions in the MTZ due to an uplifted d410 and depressed d660, and hotter areas normally correspond to a depressed d410 and uplifted d660, leading a thinner than normal MTZ (Helffrich, 2000; Ito & Katsura, 1989; Ringwood, 1975). In addition to temperature variations, the existence of water in the MTZ plays a significant role in the depth of the mineral phase changes. Experimental studies have shown that water has similar effects as low temperature on the topography of the d410 and d660 (Litasov et al., 2005; Smyth & Frost, 2002). An increase of about 1% in water content leads to an approximately 14 km increase in the MTZ thickness (Ohtani & Litasov, 2006).

The only existing MTZ study on a regional scale for Alaska was conducted by Ai et al. (2005), for the area of $-154°$ to $-146°$E and 61° to 66°N. Using teleseismic data recorded at 36 stations from different networks, 1804 receiver functions (RFs) were obtained and stacked in circular bins with a radius of 120 km. Their results show a varied d410 and d660 topography, and an overall normal d410 and elevated d660, leading to a 20–30 km thinning of the MTZ in most of the study area, which was attributed to a 100–200 K higher than normal MTZ temperature (Ai et al., 2005).

This study represents the spatially most extensive *P*-to-*S* receiver function (RF) study for Alaska and adjacent areas, by taking advantage of the dramatically increased spatial coverage of high-quality broadband seismic data recorded since the study of Ai et al. (2005), which covered approximately 20% of the area investigated by this study. We aim to provide constraints on the lateral and depth extents of the subducted slabs and the LVZ by using about 42 times more RFs than the most recent previous MTZ study for Alaska (Ai et al., 2005).

## 2. Data and Methods

The teleseismic data utilized in this study were obtained from the Incorporated Research Institutions for Seismology (IRIS) Data Management Center. We requested all the available broadband seismic data recorded by seismic stations in the area of 50°N to 73°N and −177°E to −124°E. The seismograms were recorded by both portable and permanent stations including 95 stations from the recently deployed USArray Transportable Array (TA) stations, for the recording period between early 1987 and late 2016. The epicentral distance range for selecting the teleseismic events is 30° to 100°, and the cutoff magnitude of the events is computed using an empirical formula that takes account of the epicentral distance and focal depth to balance the quality and quantity of the requested data (Liu & Gao, 2010).

The procedure for data processing, selection, and stacking is described in Gao & Liu (2014a, 2014b) and is briefly summarized here. The requested seismograms were band-pass filtered using a four-pole, two-pass Bessel filter with corner frequencies 0.02 and 0.2 Hz. Testing using a higher-corner frequency of 0.3 Hz led to almost identical results. All the filtered seismograms with signal-to-noise ratios (SNR) of the first arrival $\geq 4$ on the vertical



**Figure 3.** An azimuthal equidistant projection map centered at the study area illustrating the distribution of earthquakes used in the study. Each colored dot (radius = 1°) represents the corresponding number of used receiver functions from the earthquakes in that circle. Note the nonlinear nature of the scale bar.

component were converted into radial RFs using the frequency domain water-level deconvolution procedure (Ammon, 1991; Clayton & Wiggins, 1976) with a water-level value of 0.03. An exponential weighting function centered at the theoretical *PP* arrival is used to minimize the amplitude of the *PP* arrivals prior to RF calculation for the purpose of minimizing the degenerating effect of the *PP* arrival. To ensure the quality of the results, the resulting RFs are then subjected to an SNR-based selection procedure. A total of 75,296 high-quality RFs from 5,311 events (Figure 3) recorded by 438 stations (Figure 1) was obtained.

We geographically divided the study area into circular bins with a radius of 1° (which is comparable to the radius of the first Fresnel zone of the *P*-to-*S* converted phase at the MTZ depth), and the distance between the center of the bins is 1° geographic degree, which corresponds to 111.2 km along the N-S direction and from 40 to 70 km along the E-W direction depending on the latitude. For each bin, we moveout corrected and stacked the RFs with piercing points in the bin at the depth of 535 km (the middle of the MTZ). An alternative approach is to group and stack the RFs based on the piercing point locations calculated at each of the candidate discontinuity depths (e.g., Liu et al., 2003). This latter approach might lead to biased MTZ thickness measurements in areas with strong upper mantle velocity heterogeneities such as the study area. This is primarily because under such a RF grouping approach, some of the RFs sampling one discontinuity may not sample the other. If some of those RFs travel through the area of upper mantle velocity heterogeneities, the reliability of the resulting MTZ thickness can be reduced. The approach of grouping the RFs at the middle of the MTZ used in this study ensures that for a given bin, the same RFs sampling both discontinuities also sample the same area in the upper mantle and consequently minimizes potential bias of strong upper mantle velocity heterogeneities on the resulting MTZ thickness.
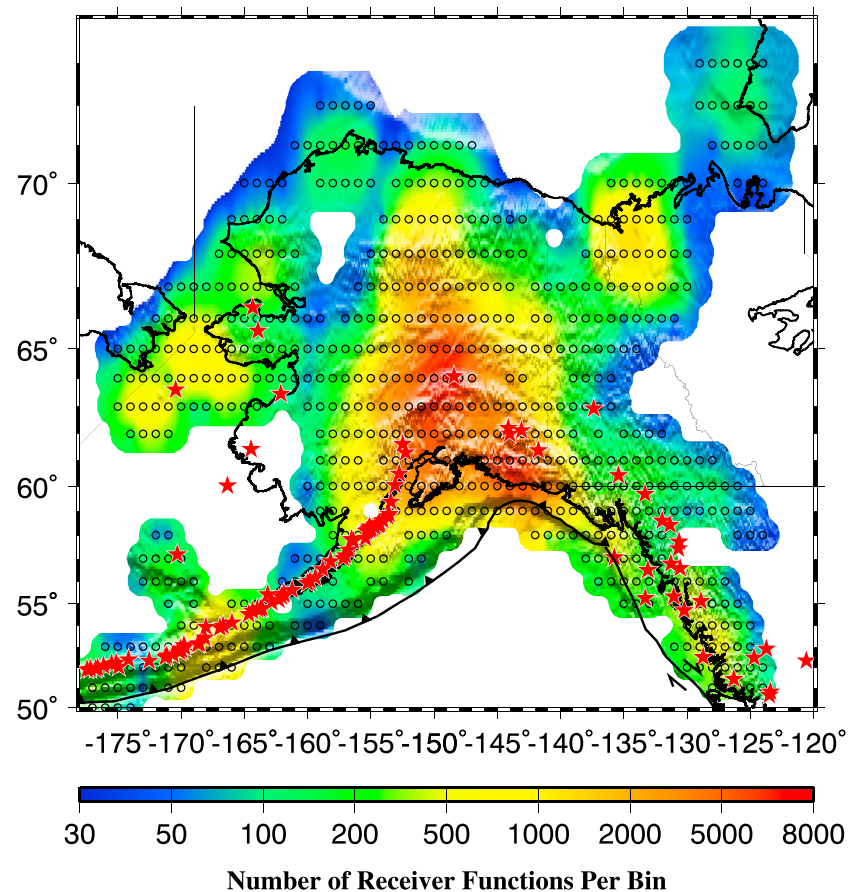
A nonplane wave assumption was used to predict the theoretical moveout times, which were computed using the IASP91 Earth model (Kennett & Engdahl, 1991). The moveout-corrected RFs were converted into depth series, for the depth range of 300–800 km with a vertical interval of 1 km. To ensure reliability, a bin was not used if the number of RFs in the bin is less than 30 (Figure 4). A bootstrap resampling procedure with 20 bootstrap iterations was applied to determine the mean and standard deviation of the MTZ discontinuity

**Figure 4.** Spatial distribution of the number of RFs in radius=1° bins. The red stars denote active volcanoes, and the black circles indicate the center of the bins with MTZ discontinuity depth measurements.

depths (Efron & Tibshirani, 1986; Liu et al., 2003). The depth series were checked visually to reject traces with weak arrivals.

## 3. Results

A total of 596 bins with prominent arrivals of either $d410$ or $d660$ was obtained. Among these bins, 536 and 505 possess clear $d410$ and $d660$ arrivals, respectively, and 445 have both reliable $d410$ and $d660$ arrivals. Figure 5 shows example cross sections of the resulting depth series for bins along two latitudinal lines and Figure S1 in the supporting information shows all of the 596 resulting depth series plotted along 24 latitudinal profiles (from 50°N to 73°N with an increment of 1°). Table S1 shows detailed information about each of the 596 bins, including the location, resulting discontinuity depths and MTZ thickness, number of RFs, and the geographic region that the bin belongs to.

### 3.1. Spatial Variation of the Apparent Discontinuity Depths

The resulting depth series reveal robust *P*-to-*S* conversions from the $d410$ and $d660$, which are most clearly observed when the traces are sorted based on the apparent depths of the $d410$ (Figure 6a) or $d660$ (Figure 6b) arrivals. On a small fraction of the time series, relatively robust multiple arrivals of the $d410$ or $d660$ are observed. In such cases, we select the arrival that has a similar shape and depth with the nearby bins (Figure S1). A continuous curvature surface gridding algorithm with a tension factor of 0.5 (Smith & Wessel, 1990) is used to produce spatially continuous images for the observed $d410$ and $d660$ depths and MTZ thickness (Figure 7), and areas with a distance greater than 1.5° from the nearest bin are masked.

Because a 1-D Earth model rather than a realistic 3-D model is used to produce the results shown in Figure 7, the resulting depths of the $d410$ and $d660$ are apparent rather than true depths. The apparent depths are functions of both the true depths of the discontinuities and velocity anomalies above the discontinuities.
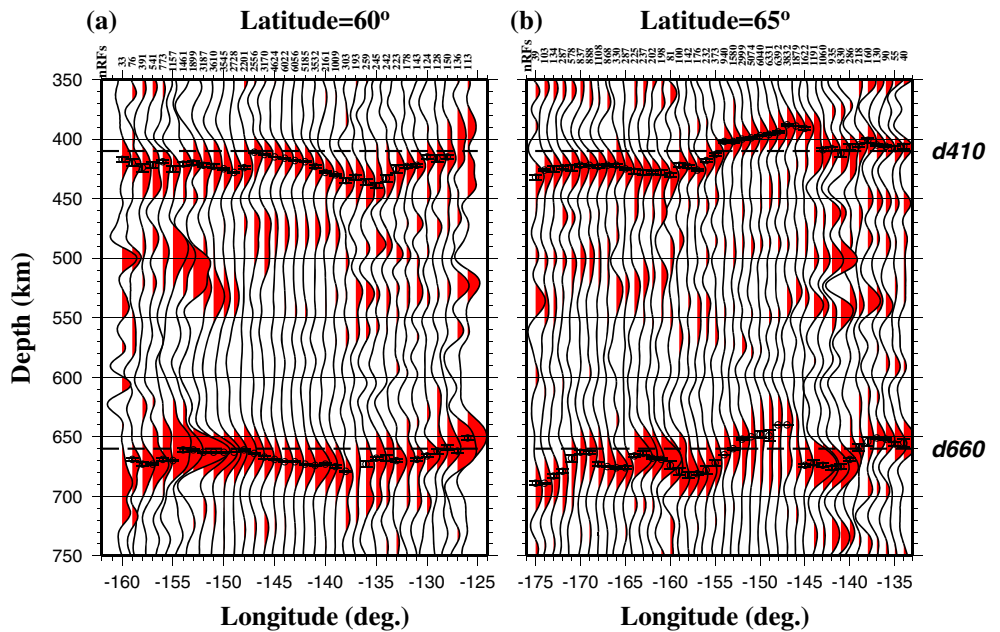
**Figure 5.** Depth series from stacking of RFs in radius = 1° bins along the (a) 60°N and (b) 65°N profiles. The circles indicate the average depths of the $d$410 and $d$660 from bootstrap resampling, and the error bars show two standard deviations of the depths. The number of RFs in each of the bins is indicated by the number atop each trace.

Velocity anomalies in the crust and upper mantle (i.e., above the $d$410) affect both the apparent depths of $d$410 and $d$660 almost equally and consequently lead to highly correlated apparent depth variations. High-velocity anomalies artificially uplift both discontinuities, and vice versa. In contrast, anomalies in the MTZ only affect the apparent depths of the $d$660. For the majority of the study area, the depths of the $d$410 and $d$660 are well correlated (Figure 8), suggesting that the observed spatial variations of the apparent depths are mostly caused by lateral velocity heterogeneities in the upper mantle.
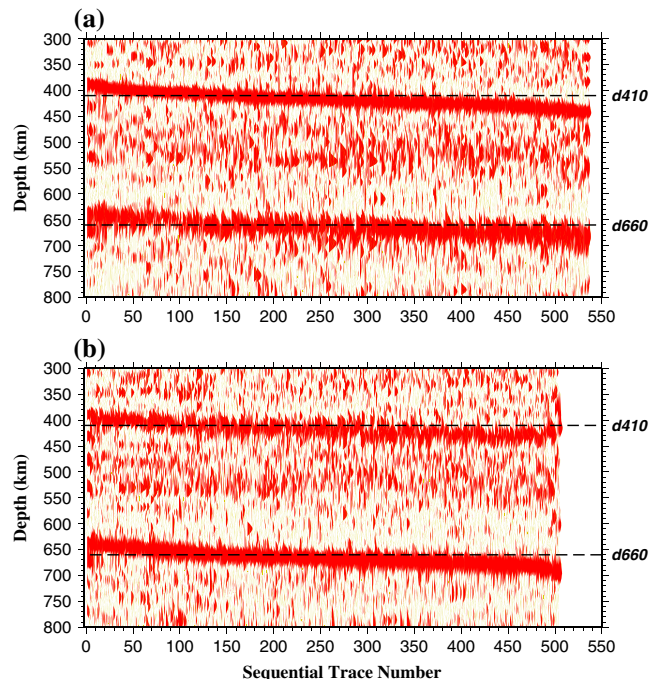


**Figure 6.** (a) Resulting depth series for each of the bins with one or two observable MTZ discontinuities, plotted with sequentially increasing depth of the $d$410. (b) Same as Figure 6a but for sequentially increasing depth of the $d$660.
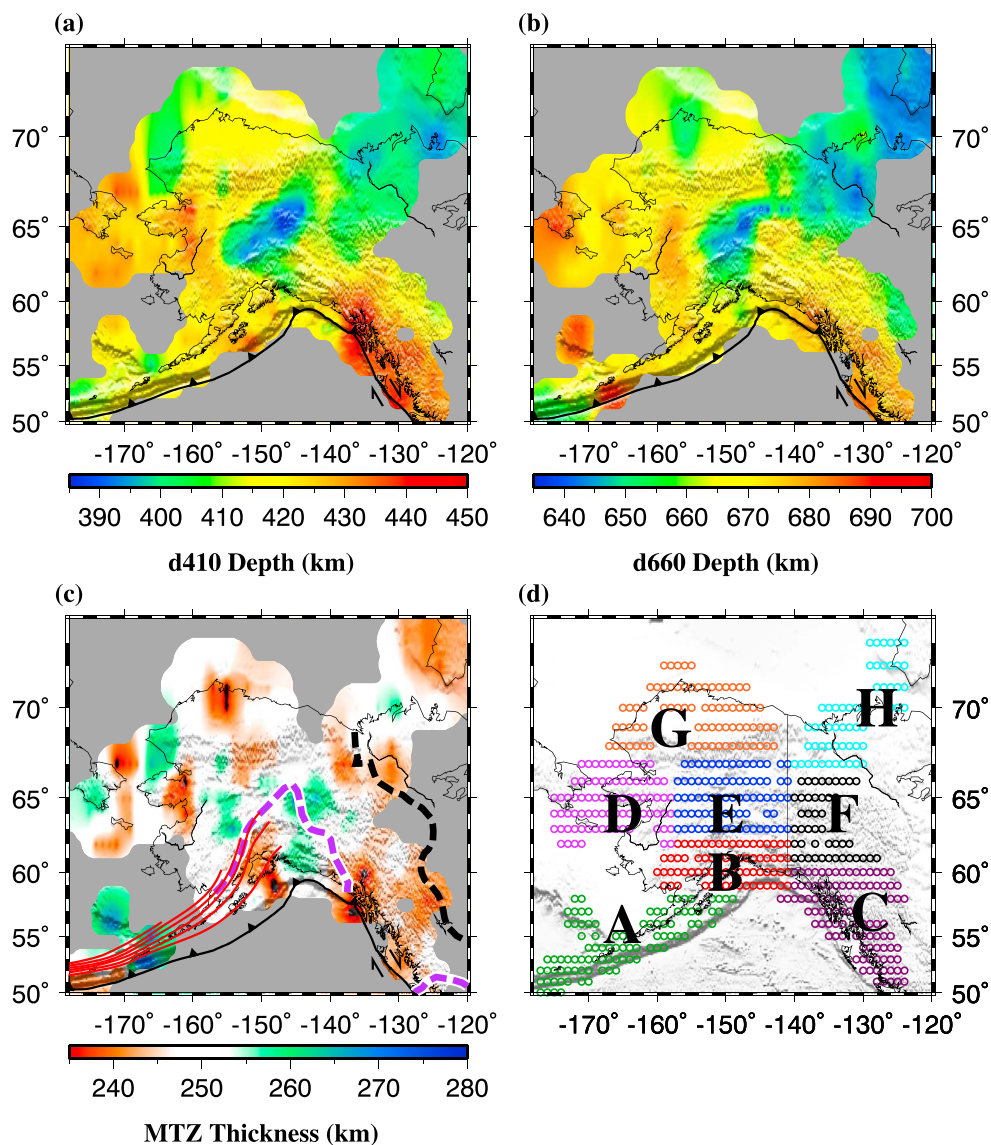
**Figure 7.** (a) Spatial distribution of apparent *d*410 depth measurements obtained using the 1-D IASP91 Earth model. (b) Same as Figure 7a but for the *d*660. (c) Apparent MTZ thicknesses. For Figure 7c, values within ±5 km from the global average are shown as white. (d) Division of the area into eight regions. Each region is indicated by differently colored circles representing the center of the bins.

The mean apparent depths of the *d*410 and *d*660 for the entire study area are 417 ± 12 and 665 ± 12 km, respectively, and the thickness of the MTZ ranges from 226 to 282 km with a mean of 248 ± 8 km, which is almost identical to the normal value of 250 km in the IASP91 Earth model (Kennett & Engdahl, 1991). We divide the study area into eight regions (Figure 7d) on the basis of the characteristics of the discontinuity depth and MTZ thickness measurements as well as known mantle velocity and tectonic provinces. The averaged apparent depths and thicknesses for each region can be found in Table 1.

Along the Aleutian Arc (Region A), the *d*410 is normal to slightly depressed with a mean apparent depth of 417 ± 7 km, and the *d*660 is depressed with a mean of 670 ± 12 km (Figure 7). The MTZ thickness in this region ranges from normal to thicker than normal with a mean value of 255 ± 10 km. The western part of this area shows an approximately 15 km thickening of the MTZ. Beneath southern Alaska (Region B), the MTZ thickness is bipolar. It is about 8 km thinner than normal in the western half and is several kilometers thicker than normal in the east.
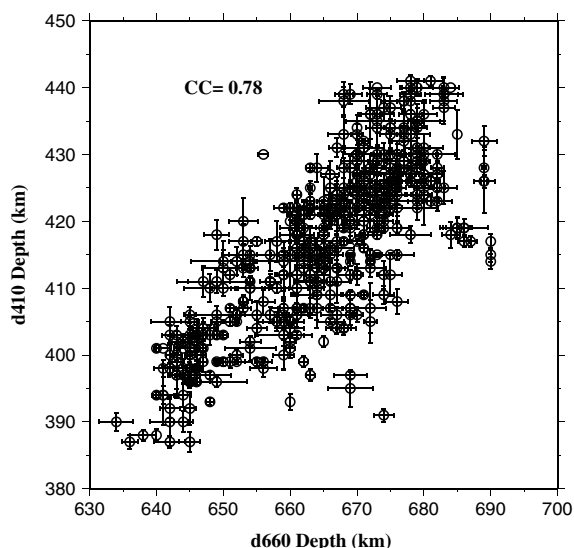
**Figure 8.** Apparent depths of the $d$410 plotted against apparent depths of the $d$660. CC: Correlation Coefficient.

The area above the proposed NCSW (Region C) is featured by significantly depressed $d$410 and $d$660, with mean apparent depths of 431±9 and 673± 9 km. The thinnest MTZ in this area is 229 km, which is 21 km thinner than the global average of 250 km, mostly due to a greater apparent depression of the $d$410 (Figure 7a) relative to that of the $d$660 (Figure 7b). Both the $d$410 and $d$660 beneath western Alaska and adjacent areas (Region D) are deeper than normal with spatially varying MTZ thicknesses. Due to the low number of RFs (Figure 4), the results for this area have large uncertainties.

Central Alaska (Region E) is sufficiently sampled by the RFs (Figure 4) and is characterized by apparently uplifted $d$410 and $d$660 for most of the area. In this area, the MTZ thicknesses range from 240 to 282 km. Spatially, this area is dominated by patches of thicker than normal MTZ thicknesses, except for the southern margin, where a thin MTZ is observed (Figure 7c). Beneath the Wrangellia Terrane and adjacent areas (Region F), the $d$410 and $d$660 are both normal, resulting in a normal MTZ thickness. Northern Alaska (Region G) is featured by normal depth and thickness measurements. Like Region D, the number of RFs per bin for this region is among the lowest in the study area (Figure 4) and thus the thin MTZ observed in the central part of this area may or may not be a real anomaly.

The North American Craton (Region H) is dominated by shallower than normal apparent discontinuity depths, with mean values of 401 ± 5 and 646 ± 4 km for the $d$410 and $d$660, respectively, leading to a statistically normal mean MTZ thickness of 246 ± 6 km. The equal-amount apparent uplift of both discontinuities is consistent with the high-velocity anomalies of the upper mantle that were mapped beneath this region (Qi et al., 2007).

### 3.2. Velocity-Corrected Depths

In order to convincingly convert the apparent depths obtained using the 1-D IASP91 Earth model discussed above into true depths, accurately determined 3-D velocity models for both $V_p$ and $V_s$ with sufficient spatial resolution for the crust, upper mantle, and MTZ are required. Results from the recent work of Martin-Short et al. (2016), which is so far the only study that has utilized the newly recorded USArray TA data and simultaneously obtained both $V_p$ and $V_s$ anomalies, are ideal for making the corrections but only for the central part of the area investigated by this study (Figure 2). The procedure that we used here to make the corrections is identical to that of Gao and Liu (2014b) used for correcting the MTZ discontinuity beneath the contiguous United States. To perform the correction, 3-D $P$ and $S$ wave velocity anomalies are interpolated into layers of 10 km thickness for the depth range of 0–700 km, and the average absolute velocity anomalies for each depth in each of the bins are calculated. The apparent depths are converted into the true depths by applying equation (8) in Gao and Liu (2014a).

Comparing the velocity-corrected depths (Figures 9a and 9b) with the apparent depths (Figures 7a and 7b), it is clear that the overall magnitude of the depth undulations is reduced for most of the areas. However,

**Table 1**
*Mean Measurements for the Eight Subregions*

| Region | $d$410 depth (km) | $\sigma_{d410}$ (km) | $d$660 depth (km) | $\sigma_{d660}$ (km) | MTZ thickness (km) | $\sigma_{MTZ}$ (km) | No. of bins |
|---|---|---|---|---|---|---|---|
| A | 417.1 | 7.1 | 670.1 | 12.1 | 254.6 | 10.3 | 50 |
| B | 418.4 | 6.3 | 666.6 | 6.8 | 247.7 | 7.4 | 59 |
| C | 431.3 | 8.6 | 673.2 | 8.7 | 242.6 | 4.8 | 62 |
| D | 426.3 | 6.5 | 674.1 | 5.5 | 247.8 | 8.1 | 72 |
| E | 406.6 | 12.6 | 660.2 | 12.6 | 252.2 | 8.0 | 67 |
| F | 412.0 | 9.3 | 661.1 | 9.9 | 247.6 | 5.1 | 38 |
| G | 413.9 | 7.1 | 662.4 | 5.5 | 247.1 | 7.2 | 46 |
| H | 400.5 | 4.6 | 646.2 | 4.4 | 245.6 | 5.5 | 51 |
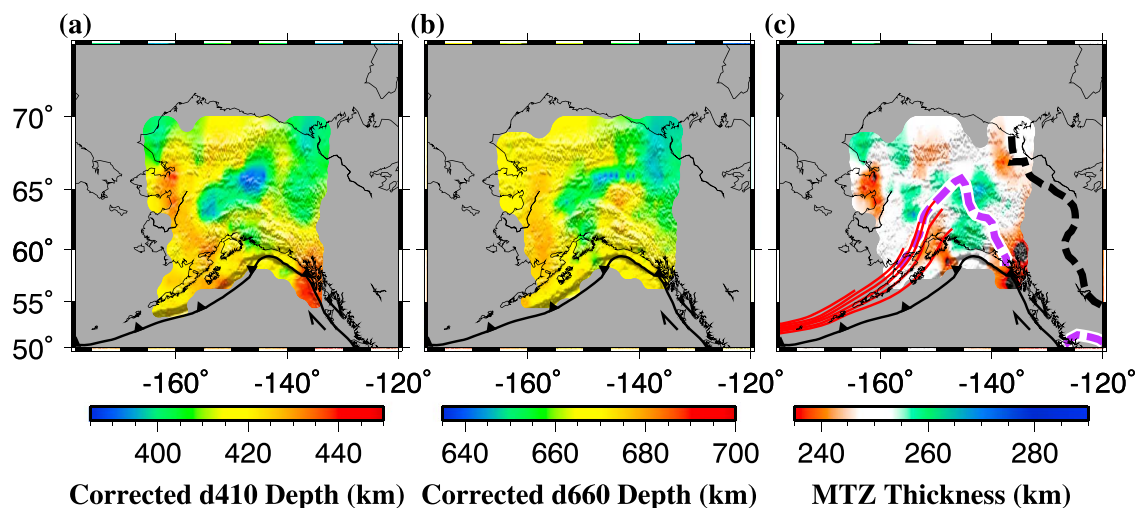
**Figure 9.** (a) Corrected *d*410 depth for the area covered by the study of Martin-Short et al. (2016). (b) Same as Figure 9a but for the *d*660. (c) Corrected MTZ thickness measurements.

the corrected *d*410 and *d*660 depths are still positively correlated, with a correlation coefficient of 0.69. Although this is smaller than the original value of 0.78, the positive correlation between the corrected depths of the *d*410 and *d*660 possibly suggests that the magnitude of the velocity anomalies in the velocity models is underestimated for the area.

## 4. Discussion

### 4.1. Implications for the Depth and Lateral Extents of Subducted Slabs

As demonstrated by numerous previous studies in the vicinity of modern or ancient subduction zones (e.g., Contenti et al., 2012; Liu et al., 2003, 2016), the relationship between the depths (both the apparent and corrected) of the two MTZ discontinuities and the MTZ thicknesses can provide valuable constraints to the depth extent of cold slab segments and the existence of zones of high water content in the MTZ. For the study area, seismic tomographic images have suggested the existence of cold slab segments beneath the Aleutians and central Alaska (Burdick et al., 2017; Martin-Short et al., 2016; Qi et al., 2007; Zhao et al., 1995), with contradictory conclusions about their depth of penetration. In this section, we speculate their depth extent using the observed MTZ discontinuity undulations.

The presence of a cold slab only in the upper mantle (Situation A) leads to highly correlated apparent uplifts of both discontinuities and a normal MTZ thickness. If the velocity correction is accurate, the apparent uplifts of the discontinuities diminish, and the MTZ thicknesses remain normal. This is probably not the case for both the Aleutians (Region A) and central Alaska (Region E), beneath which areas a thicker than normal MTZ is observed (Figures 7c and 9c).

If a slab penetrates the upper mantle and the entire MTZ (Situation B), the resulting apparent and corrected depths of the *d*410 are shallower than normal, due to both the higher upper mantle velocities and the lower temperature in the upper MTZ which uplift the *d*410. The behavior of the *d*660, however, is dependent on the competing effects of the higher upper mantle and MTZ velocities (which lead to an apparent uplift for the *d*660) and the negative temperature anomaly at the bottom of the MTZ (which results in its depression due to the negative Clapeyron slope). Previous MTZ discontinuity studies for other modern subduction zones with confirmed existence of slabs in the lower MTZ showed that the temperature effect usually overcomes the effect of higher velocities, leading to deeper than normal apparent depths of the *d*660 (Contenti et al., 2012; Liu et al., 2003, 2016), which are not observed in areas with tomographically inferred slab segments.

A slab extending from the upper mantle to the upper MTZ (Situation C) leads to a greater apparent uplift of the *d*410 than the *d*660, due to the thermal effect of the slab on the former. The low temperature is also responsible for a thicker than normal MTZ. After the velocity correction, the depth of the *d*660 becomes normal and that for the *d*410 remains uplifted with a reduced magnitude relative to the apparent depth. For central Alaska, although Situation B cannot be completely ruled out due to uncertainties in the accuracy

of the velocity anomalies, our measurements fit Situation C, that is, cold slab segments are mostly concentrated in the upper MTZ, the best. This conclusion is consistent with both the recent tomographic studies shown in Figure 2, in which only minor high-velocity anomalies are imaged in the lower MTZ. If this is the case, the minor high-velocity anomalies in the lower MTZ might be due to vertical smearing (Frederiksen et al., 1998; Martin-Short et al., 2016). Alternatively, this could indicate greatly reduced temperature contrast between the slab segments and the ambient mantle. Unlike the mostly planar pattern of the slab in the upper mantle shown in the tomographic images (Figure 2), the subducted slab seems segmented and spreading over a broader area in the MTZ (Figure 7c), including directly beneath the trench in southern Alaska (eastern half of Region B) and central Alaska (Region E). In addition, the thicker than normal MTZ beneath the Aleutians (Region A) might be indicative of the existence of cold slab segments in the MTZ, which is consistent with results from seismic tomography studies (Figures 2b and 2c) (Burdick et al., 2017).

While in principle the existence of hydrous mineral phases within the MTZ could affect the topography of both MTZ discontinuities by uplifting the $d$410 and depressing the $d$660 (Ohtani & Litasov, 2006; Ghosh et al., 2013), it is unlikely for the study area because (1) the presence of an anomalously large amount of water in the MTZ should result in a reduction of seismic velocities, which is inconsistent with the most recent tomographic studies (Figure 2), and (2) water should lead to a reduction of the amplitude of the $d$410 by broadening the vertical distance for the olivine-spinel phase transition. Such a reduction is not observed for central Alaska and the Aleutians (Figures 5 and S1).

### 4.2. Causes of the LVZ Above Slab Windows

One of the most prominent features in our results is the highly depressed $d$410 beneath the NCSW (Region C in Figure 7). In the tomographic images of Burdick et al. (2017), the low velocities in this area are mostly limited in the upper mantle, while Martin-Short et al. (2016) suggested that at least the NW part of this LVZ extends to the lower MTZ (Figure 2f). In this area, the maximum apparent depression of the $d$410 is located at 137°W by 58°N, with an amplitude of 31 km. At the same location, the apparent depression of the $d$660 is 18 km, leading to a 13 km apparent thinning of the MTZ. After velocity correction, the corresponding values are 26, 11, and 15 km, respectively (Figure 9). If we assume that the 15 km MTZ thinning is solely from the depression of the $d$410, a 182 K thermal anomaly in the upper MTZ is required to produce the depression for an assumed Clapeyron slope of 2.9 MPa/K (Bina & Helffrich, 1994). Using a scaling factor of $dV_p/dT = -4.8 \times 10^{-4}$ km s$^{-1}$ $K^{-1}$ (Deal et al., 1999), this temperature anomaly causes a $-1\%$ velocity anomaly, which is comparable to the value reported by Martin-Short et al. (2016) (Figure 2e).

The observation that the upper MTZ is hotter than normal provides constraints on a number of previously proposed models for the formation mechanism of this LVZ. First, as suggested by Frederiksen et al. (1998), lithospheric collision-induced strain heating (Kincaid & Silver, 1996) cannot explain the LVZ, because it only affects the temperature of the upper 100 km of the mantle. Second, the LVZ is unlikely to be related to a mantle plume originating from the lower mantle, which is a frequently used hypothesis to explain upper mantle low-velocity anomalies (e.g., Montelli et al., 2004). A plume origin of the Anahim volcanic track (which is approximately located at about 125°W and 52°N) in the study area has been suggested (Mercier et al., 2009). The plume model would predict a shallowing of the $d$660, which is not observed in the area covered by this study (Figures 7b and 9c). However, the true depth of the $d$660 cannot be obtained at the present time for the Anahim volcanic track area (Figure 7b) due to a lack of $V_p$ and $V_s$ velocity models, and thus, whether there is a plume beneath the volcanic track remains unresolved. Third, the observations provide supporting evidence for the model involving advective upflow of hot material through the NCSW (Thorkelson et al., 2011; Frederiksen et al., 1998). The reduced pressure in the slab window resulted in decompression partial melting and is responsible for the observed volcanism and upper mantle LVZ in the area. Results from this study are consistent with the hypothesis that the upflow is capable of causing significant temperature anomalies in areas as deep as at least the upper MTZ. Thermal upwelling through a slab window has been proposed beneath some other areas such as the Indochina Peninsula (Yu et al., 2017) and SW China (Zhang et al., 2017) and is considered to be the upwelling component of a return flow system induced by sinking slab segments, as revealed by geodynamic modeling (Faccenna et al., 2010).

## 5. Conclusions

The resulting highly correlated apparent $d$410 and $d$660 depths (Figure 8) suggest strong upper mantle velocity heterogeneities corresponding to subducted slabs beneath central Alaska and an advective thermal

upwelling through a slab window in the Northern Cordillera. This study confirms the existence of a subducted cold slab beneath central Alaska in the upper mantle and provides independent evidence for its penetration into the upper MTZ, where the slab is probably broken into fragments. Our results show that the LVZ observed above the Northern Cordilleran slab window extends to the upper MTZ, where the observed depression of the $d410$ corresponds to a thermal anomaly of about 180 K.

## References

Ai, Y., Zhao, D., Gao, X., & Xu, W. (2005). The crust and upper mantle discontinuity structure beneath Alaska inferred from receiver functions. *Physics of the Earth and Planetary Interiors*, *150*(4), 339–350. https://doi.org/10.1016/j.pepi.2004.12.002

Ammon, C. (1991). The isolation of receiver effects from teleseismic *P*-wave forms. *Bulletin of the Seismological Society of America*, *81*, 2504–2510.

Anderson, D. L. (1967). Phase changes in the upper mantle. *Science*, *157*, 1165–1173.

Bina, C. R., & Helffrich, G. (1994). Phase transition Clapeyron slopes and transition zone seismic discontinuity topography. *Journal of Geophysical Research*, *99*, 15,853–15,860.

Burdick, S., Vernon, F. L., Martynov, V., Eakins, J., Cox, T., Tytell, J., . . . van der Hilst, R. D. (2017). Model update May 2016: Upper-mantle heterogeneity beneath North America from travel-time tomography with global and USArray data. *Seismological Research Letters*, *88*, 319–325. https://doi.org/10.1785/0220160186

Clayton, R. W., & Wiggins, R. A. (1976). Source shape estimation and deconvolution of teleseismic bodywaves. *Geophysical Journal International*, *47*, 151–177. https://doi.org/10.1111/j.1365-246X.1976.tb01267.X

Collier, J. D., Helffrich, G. R., & Wood, B. J. (2001). Seismic discontinuities and subduction zones. *Physics of the Earth and Planetary Interiors*, *127*, 35–49.

Contenti, S., Gu, Y. J., Okeler, A., & Sacchi, M. D. (2012). Shear wave reflectivity imaging of the Nazca-South America subduction zone: Stagnant slab in the mantle transition zone? *Geophysical Research Letters*, *39*, L02310. https://doi.org/10.1029/2011GL050064

Deal, M. M., Nolet, G., & van der Hilst, R. D. (1999). Slab temperature and thickness from seismic tomography: 1. Method and application to Tonga. *Journal of Geophysical Research*, *104*, 28,789–28,802.

DeMets, C., Gordon, R. G., Argus, D. F., & Stein, S. (1990). Current plate motions. *Geophysical Journal International*, *101*, 425–478. https://doi.org/10.1111/j.1365-246X.1990.tb06579.X

Eberhart-Phillips, D., Christensen, D. H., Brocher, T. M., Hansen, R., Ruppert, N. A., Haeussler, P. J., & Abers, G. A. (2006). Imaging the transition from Aleutian subduction to Yakutat collision in central Alaska, with local earthquakes and active source data. *Journal of Geophysical Research*, *111*, B1303. https://doi.org/10.1029/2005JB004240

Efron, B., & Tibshirani, R. (1986). Bootstrap methods for standard errors, confidence intervals, and other measures of statistical accuracy. *Statistical Science*, *1*, 54–75.

Faccenna, C., Becker, T. W., Lallenmand, S., Lagabrielle, Y., Funiciello, F., & Piromallo, C. (2010). Subduction-triggered magmatic pulses: A new class of plumes? *Earth and Planetary Science Letters*, *299*, 54–68. https://doi.org/10.1016/j.epsl.2010.08.012

Fei, Y., Van Orman, J., Li, J., Van Westrenen, W., Sanloup, C., Minarik, W., & Funakoshi, K. I. (2004). Experimentally determined postspinel transformation boundary in $Mg_2SiO_4$ using MgO as an internal pressure standard and its geophysical implications. *Journal of Geophysical Research*, *109*, B02305. https://doi.org/10.1029/2003JB002562

Fisher, M. A., & Magoon, L. B. (1978). Geologic framework of lower Cook Inlet. *American Association of Petroleum Geologists Bulletin*, *62*(3), 373–402.

Foulger, G. R., Panza, G. F., Artemieva, I. M., Bastow, I. D., Cammarano, F., Doglioni, C., . . . Yanovskaya, T. B. (2015). What lies deep in the mantle below? *Eos Earth & Space Science News*, *96*, 1–7.

Frederiksen, A. W., Bostock, M. G., VanDecar, J. C., & Cassidy, J. F. (1998). Seismic structure of the upper mantle beneath the northern Canadian Cordillera from teleseismic travel-time inversion. *Tectonophysics*, *294*, 43–55.

Fukao, Y., Widiyantoro, S., & Obayashi, M. (2001). Stagnant slabs in the upper and lower mantle transition region. *Reviews of Geophysics*, *39*, 291–323. https://doi.org/10.1029/1999RG000068

Gao, S. S., & Liu, K. H. (2014a). Imaging mantle discontinuities using multiply-reflected *P*-to-*S* conversions. *Earth and Planetary Science Letters*, *402*, 99–106. https://doi.org/10.1016/j.epsl.2013.08.025

Gao, S. S., & Liu, K. H. (2014b). Mantle transition zone discontinuities beneath the contiguous United States. *Journal of Geophysical Research: Solid Earth*, *119*, 6452–6468. https://doi.org/10.1002/2014JB011253

Ghosh, S., Ohtani, E., Litasov, K. D., Suzuki, A., Dobson, D., & Funakoshi, K. (2013). Effect of water in depleted mantle on post-spinel transition and implication for 660 km seismic discontinuity. *Earth and Planetary Science Letters*, *371–372*, 103–111. https://doi.org/10.1016/j.epsl.2013.04.011

Goes, S., Agrusta, R., van Hunen, J., & Garel, F. (2017). Subduction-transition zone interaction: A review. *Geosphere*, *13*, 644–664. https://doi.org/10.1130/GES01476.1

Gudmundsson, O., & Sambridge, M. (1998). A regionalized upper mantle (RUM) seismic model. *Journal of Geophysical Research*, *103*, 7121–7136.

Helffrich, G. (2000). Topography of the transition zone seismic discontinuities. *Reviews of Geophysics*, *38*, 141–158. https://doi.org/10.1029/1999RG000060

Ito, E., & Katsura, T. (1989). A temperature profile of the mantle transition zone. *Geophysical Research Letters*, *16*, 425–428.

Katsura, T., Yamada, H., Shinmei, T., Kubo, A., Ono, S., Kanzaki, M., . . . Utsumi, W. (2003). Post-spinel transition in $Mg_2SiO_4$ determined by high P-T in situ X-ray diffractometry. *Physics of the Earth and Planetary Interiors*, *136*, 11–24. https://doi.org/10.1016/S0031-9201(03)00019-0

Kennett, B. L. N., & Engdahl, E. R. (1991). Traveltimes for global earthquake location and phase identification. *Geophysical Journal International*, *105*, 429–465. https://doi.org/10.1111/j.1365-246X.1991.tb06724.x

Kennett, B. L. N., Engdahl, E. R., & Buland, R. (1995). Constraints on seismic velocities in the Earth from traveltimes. *Geophysical Journal International*, *122*, 108–124.

Kincaid, C., & Silver, P. G (1996). The role of viscous dissipation in the orogenic process. *Earth and Planetary Science Letters*, *142*, 271–288. https://doi.org/10.1016/0012-821X(96)00116-1

Li, C., van der Hilst, R. D., Engdahl, E. R., & Burdick, S. (2008). A new global model for P wave speed variations in Earth's mantle. *Geochemistry, Geophysics, Geosystems*, *9*, Q05018. https://doi.org/10.1029/2007GC001806

Li, X., & Yuan, X. (2003). Receiver functions in northeast China—Implications for slab penetration into the lower mantle in northwest Pacific subduction zone. *Earth and Planetary Science Letters*, *216*, 679–691. https://doi.org/10.1016/S0012-821X(03)00555-7

Litasov, K. D., Ohtani, E., Sano, A., Suzuki, A., & Funakoshi, K. (2005). Wet subduction versus cold subduction. *Geophysical Research Letters*, *32*, L13312. https://doi.org/10.1029/2005GL022921

Liu, K. H., & Gao, S. S. (2010). Spatial variations of crustal characteristics beneath the Hoggar swell, Algeria, revealed by systematic analyses of receiver functions from a single seismic station. *Geochemistry, Geophysics, Geosystems*, *11*, Q08011. https://doi.org/10.1029/2010GC003091

Liu, K. H., Gao, S. S., Silver, P. G., & Zhang, Y. K. (2003). Mantle layering across central South America. *Journal of Geophysical Research*, *108*(B11), 2510. https://doi.org/10.1029/2002JB002208

Liu, Z., Niu, F., Chen, Y. J., Grand, S., Kawakatsu, H., Ning, J., . . . Ni, J. (2016). Receiver function images of the mantle transition zone beneath NE China: New constraints on intraplate volcanism, deep subduction and their potential link. *Earth and Planetary Science Letters*, *412*, 101–111. https://doi.org/10.1016/j.epsl.2014.12.019

Martin-Short, R., Allen, R. M., & Bastow, I. D. (2016). Subduction geometry beneath south central Alaska and its relationship to volcanism. *Geophysical Research Letters*, *43*, 9509–9517. https://doi.org/10.1002/2016GL070580

Mercier, J.-P., Bostock, M. G., Cassidy, J. F., Dueker, K., Gaherty, J. B., Garnero, E. J., . . . Zandt, G. (2009). Body-wave tomography of western Canada. *Tectonophysics*, *475*, 480–492. https://doi.org/10.1016/j.tecto.2009.05.030

Montelli, R., Nolet, G., Dahlen, F. A., Masters, G., Engdahl, E. R., & Hung, S. H. (2004). Finite-frequency tomography reveals a variety of plumes in the mantle. *Science*, *303*, 338–343. https://doi.org/10.1126/science.1092485

Ohtani, E., & Litasov, K. D. (2006). The effect of water on mantle phase transitions. In H. Keppler & J. R. Smyth (Eds.), *Water in Normially Anhydrous Minerals, Reviews in Mineralogy and Geochemistry* (Vol. 62, pp. 397–419). Washington, DC: Mineralogical Society of America. https://doi.org/10.2138/rmg.2006.62.17

Page, R. A., Plafker, G., & Pulpan, H. (1995). Block rotation in east-central Alaska: A framework for evaluating earthquake potential? *Geology*, *23*, 629–632. https://doi.org/10.1130/0091-7613(1995)023<0629:BRIECA>2.3.CO;2

Page, R. A., Stephens, C. D., & Lahr, J. C. (1989). Seismicity of the Wrangell and Aleutian Wadati-Benioff zones and the North American plate along the Trans-Alaska crustal transect, Chugach Mountains and Copper River basin, southern Alaska. *Journal of Geophysical Research*, *94*, 16,059–16,082. https://doi.org/10.1029/JB094iB11p16059

Qi, C., Zhao, D., & Chen, Y. (2007). Search for deep slab segments under Alaska. *Physics of the Earth and Planetary Interiors*, *165*, 68–82. https://doi.org/10.1016/j.pepi.2007.08.004

Ringwood, A. E. (1975). *Composition and petrology of the Earth's mantle*. New York: McGraw-Hill.

Schaeffer, A. J., & Lebedev, S. (2014). Imaging the North American continent using waveform inversion of global and USArray data. *Earth and Planetary Science Letters*, *402*, 26–41. https://doi.org/10.1016/j.epsl.2014.05.014

Shearer, P. M., & Masters, T. G. (1992). Global mapping of topography on the 660-km discontinuity. *Nature*, *355*, 791–796.

Smith, W. H. F., & Wessel, P. (1990). Gridding with continuous curvature splines in tension. *Geophysics*, *55*, 293–305.

Smyth, J. R., & Frost, D. J. (2002). The effect of water on the 410-km discontinuity: An experimental study. *Geophysical Research Letters*, *29*, 1485. https://doi.org/10.1029/2001GL014418

Taber, J. J., Billington, S., & Engdahl, E. R. (1991). Seismicity of the Aleutian Arc. In D. B. Slemmons, et al. (Eds.), *Neotectonics of North America* (pp. 29–46). Boulder, CO: Geological Society of America.

Thorkelson, D. J., Madsen, J. K., & Sluggett, C. L. (2011). Mantle flow through the Northern Cordilleran slab window revealed by volcanic geochemistry. *Geology*, *39*, 267–270. https://doi.org/10.1130/G31522.1

Thorkelson, D. J., & Taylor, R. P. (1989). Cordilleran slab windows. *Geology*, *17*, 833–836. https://doi.org/10.1130/0091-7613(1989)017<0833:CSW>2.3.CO;2

Wang, Y., & Tape, C. (2014). Seismic velocity structure and anisotropy of the Alaska subduction zone based on surface wave tomography. *Journal of Geophysical Research: Solid Earth*, *119*, 8845–8865. https://doi.org/10.1002/2014JB011438

Wicks Jr., C. W., & Richards, M. A. (1993). A detailed map of the 660-kilometer discontinuity beneath the Izu-Bonin subduction zone. *Science*, *261*, 1424–1427.

Yamazaki, D., & Karato, S. (2001). Some mineral physics constraints on the rheology and geothermal structure of Earth's lower mantle. *American Mineralogist*, *86*, 385–391. https://doi.org/10.2138/am-2001-0401

Yu, Y., Gao, S. S., Liu, K. H., Yang, T., Xue, M., & Le, K. P. (2017). Mantle transition zone discontinuities beneath the Indochina Peninsula: Implications for slab subduction and mantle upwelling. *Geophysical Research Letters*, *44*, 7159–7167. https://doi.org/10.1002/2017GL073528

Yuan, H., & Romanowicz, B. (2010). Lithospheric layering in the North American craton. *Nature*, *466*, 1063–1068. https://doi.org/10.1038/nature09332

Zhang, R., Wu, Y., Gao, Z., Fu, Y. V., Sun, L., Wu, Q., & Ding, Z. (2017). Upper mantle discontinuity structure beneath eastern and southeastern Tibet: New constraints on the Tengchong intraplate volcano and signatures of detached lithosphere under the western Yangtze Craton. *Journal of Geophysical Research: Solid Earth*, *122*, 1367–1380. https://doi.org/10.1002/2016JB013551

Zhao, D., Christensen, D., & Pulpan, H. (1995). Tomographic imaging of the Alaska subduction zone. *Journal of Geophysical Research*, *100*, 6487–6504. https://doi.org/10.1029/95JB00046